

The imitation game (r)evolutions: Q-star effective shadow from GRMHD analysis

Víctor Jaramillo,^{1,2,*} Laura Meneses,^{3,†} Héctor R. Olivares Sánchez,^{4,‡}
Carlos Herdeiro,^{4,5,§} Darío Núñez,^{3,¶} and Shuang-Yong Zhou^{6,7,**}

¹*Department of Modern Physics, University of Science and Technology of China, Hefei, Anhui 230026, China*

²*Departamento de Física, Universidad de Guadalajara, 44430 Guadalajara, Jalisco, México*

³*Instituto de Ciencias Nucleares, Universidad Nacional Autónoma de México, Circuito Exterior C.U., A.P. 70-543, Coyoacán, México 04510, CdMx, México*

⁴*Departamento de Matemática da Universidade de Aveiro and Centre for Research and Development in Mathematics and Applications (CIDMA), Campus de Santiago, 3810-183 Aveiro, Portugal.*

⁵*Programa de Pós-Graduação em Física, Universidade Federal do Pará, 66075-110, Belém, Pará, Brazil.*

⁶*Interdisciplinary Center for Theoretical Study, University of Science and Technology of China, Hefei, Anhui 230026, China*

⁷*Peng Huanwu Center for Fundamental Theory, Hefei, Anhui 230026, China*

Q -stars are a class of boson stars arising in scalar-field theories with interacting potentials, minimally coupled to gravity. We show that, in certain regions of parameter space, the angular velocity of stable timelike circular geodesics around Q -stars can attain a maximum at a nonzero radius. Notably, this behaviour may occur for *stable* configurations. This feature has been argued to produce effective shadows, but so far it has only been investigated for unstable solutions. We test this possibility by performing general relativistic magnetohydrodynamic evolutions for a representative stable Q -star model. A low-density, low-luminosity central region is indeed observed to form and persist – at least until the evolution becomes affected by numerical viscosity. As a proof of principle, this suggests that families of stable bosonic stars can act as black hole mimickers. Moreover, for the model at hand, a heuristic analysis shows that the effective shadow has a comparable size to that of a Schwarzschild black hole with the same mass. Importantly, this mechanism for generating an effective shadow does not rely on the object being ultracompact, or an ad hoc chosen accretion disk.

CONTENTS

I. Introduction	2
II. Q -star spacetime	3
A. Families of Q -stars and the role of self-interactions	4
B. Selection of the configurations	4
III. General relativistic magnetohydrodynamic simulations	7
A. Simulation setup	7
B. Results	8
1. Simulation results	8
2. Numerical viscosity and lifetime of the central hollow	10
3. Observational considerations	12
IV. Discussion and conclusions	13
Acknowledgments	14
A. Central brightness depression in the final state	14
References	14

* jaramillo@ustc.edu.cn

† laurak@ciencias.unam.mx

‡ h.sanchez@ua.pt

§ herdeiro@ua.pt

¶ nunez@nucleares.unam.mx

** zhoushy@ustc.edu.cn

I. INTRODUCTION

Observations by the Event Horizon Telescope (EHT) have opened a new window into the strong-field regime of gravity, providing horizon-scale images of compact objects and enabling direct tests of the black hole paradigm. The observation of shadow-like features in sources such as M87* and Sgr A* has intensified both theoretical and observational efforts to understand the formation and interpretation of black hole shadows, as well as to assess to what extent alternative compact objects may produce similar observational signatures. In this context, horizonless configurations that can mimic certain properties of black holes have received growing attention.

Following the fruitful developments of perturbative quantum field theory, interest in solitons within relativistic systems gained momentum. These solitons are extended, localized field configurations that are stable. Their stability may arise from topological reasons [1], or be ensured by internal symmetries. In the latter case, they are known as non-topological solitons, a class which includes Q -balls [2–4] (see [5] for a recent review). To evade Derrick’s theorem, Q -balls must be time-dependent in field space rather than static. Q -balls naturally arise in supersymmetric extensions of the Standard Model [6–8]. In the early universe, they can form as a by-product of Affleck–Dine baryogenesis [9–15], and may persist to the present day as dark matter candidates [16–24].

Q -balls form due to the attractive nature of the scalar potential. In the simplest case of a single $U(1)$ scalar field, this requires the (effective) potential to include at least a $|\Phi|^6$ term, enabling condensation within field fragments. In the presence of gravitational attraction, non-topological solitons known as boson stars [25, 26] can form even with a free scalar potential. However, such mini-boson stars are limited in compactness, at least within the stable branch [27, 28]. Including self-interactions—leading to what we refer to as Q -stars in this paper—enriches the phenomenology by increasing both the mass and the compactness of the boson star, but still allowing stable stars.

Building on the role of self-interactions in boson stars, stationary solutions supported by sextic scalar potentials have been extensively constructed and analyzed in the literature. Static, spherically symmetric configurations were first studied in [29, 30], while non-spherical solutions, such as dipolar and chain configurations, were obtained in [31, 32], including their black hole counterparts [33]. Rotating solutions were investigated in [34] and also in the case of gauge fields [35]. The stability properties of these configurations have also been explored in detail [36–38], revealing robustness against a variety of perturbations. Interestingly, spinning boson stars, which are unstable in the case of a free scalar potential, can be stabilized once suitable self-interactions—such as those of a Q -star-type potential—are included. Recent studies have also shown that these interaction terms enable a novel energy-amplification mechanism for waves scattering off Q -balls [39–43] and Q -stars [40, 41, 44], namely a superradiant process driven by internal-space rotation. Additionally, Q -balls and Q -stars can exhibit rich spatial configurations that go beyond spherical symmetry [45–49].

The possibility that boson stars may produce strong gravitational lensing has motivated early studies of their lensing properties and possible shadow-like features [50–53]. The latter raised the question whether their observational signatures may resemble those of black holes; this led to pioneering studies of such *imitation game* [53, 54], reloaded [55] and re-analysed [56, 57] in different setups to identify the conditions under which boson stars can generate central dim regions or effective shadows, even in the absence of an event horizon. These analyses highlight both similarities and qualitative differences with the standard black hole scenario, and emphasize the role played by the spacetime structure and geodesic motion, as well as the astrophysical light source, in shaping observable features. But general-relativistic magnetohydrodynamic evolutions (GRMHD) simulations, necessary to produce state of the art synthetic images in this context, were only studied in [54], where the boson star models that could mimic black hole images were unstable. Thus, it remains to see if stable boson stars could actually be players in this imitation game, under GRMHD evolutions. An affirmative answer to this question will be provided in this paper.

More broadly, boson stars belong to a larger class of horizonless or exotic compact objects that may act as black hole mimickers. These include, among others, black holes with scalar [58] or vector hair [59], Proca stars [60], and other self-gravitating solitonic configurations. Assessing the observational degeneracies and discriminating signatures among these possibilities is a central goal of current strong-gravity astrophysics.

In this work we investigate a specific mechanism through which Q -stars can produce effective shadow-like features without requiring ultracompactness (*i.e.* possessing light rings, which may source a spacetime instability [61–63] - see also [64–67] for the ongoing debate). We focus on configurations for which the angular velocity of stable timelike circular geodesics peaks at a nonzero radius and explore the observational consequences through GRMHD evolutions. Our results indicate the formation of a persistent low-density, low-luminosity central region, supporting the interpretation of Q -stars as viable black hole mimickers in certain regimes.

The remainder of this paper is organized as follows. In Sec. II we present the theoretical framework and the Q -star models under consideration and we describe the geodesic structure and the conditions leading to a non-monotonic angular velocity profile. In Sec. III we outline the GRMHD setup and numerical methodology and present our results and their observational implications. We conclude in Sec. IV with a summary and outlook.

Throughout this work we adopt the metric signature $(-, +, +, +)$ and use units in which $c = 1$. Newton’s constant

is set to $G = 1$, except in selected expressions where it is retained for clarity in the presentation of the physical model.

II. Q -STAR SPACETIME

The background spacetime for the GRMHD simulations will be that of a self-gravitating Q -ball, also known as a Q -star. These configurations, composed of a complex scalar field, can be interpreted as boson stars but with a different scalar potential compared to the simpler mini-boson stars [25, 26]. They are also referred to in the literature as soliton stars [29, 30]. In flat spacetime, one of the simplest potentials that can support Q -balls¹ is given by a complex scalar field with the potential $V(\Phi) = \mu^2|\Phi|^2 + \lambda/2|\Phi|^4 + \nu/3|\Phi|^6$. This is, in fact, the simplest polynomial potential with symmetry \mathbb{Z}_2 that supports Q -ball solutions when λ is negative. In the absence of gravitational attraction, the (nonlinear) interaction terms of the potential must drip below zero in order for Q -balls to form. Negative interaction terms effectively induce attractive forces among scalar perturbations and energetically favor localized field configurations over homogeneous ones. This is because localization allows the field to attain large amplitudes in its core, where the negative interaction terms contribute more significantly and reduce the total energy. Physically, this corresponds to particles clustering together to form bound, localized structures.

Q -stars are obtained by minimally coupling a complex scalar field to gravity, where the scalar field acts as the source of the gravitational field through the energy-momentum tensor:

$$T_{\mu\nu} = 2\partial_{(\mu}\Phi^\dagger\partial_{\nu)}\Phi - g_{\mu\nu}(\partial^\kappa\Phi^\dagger\partial_\kappa\Phi + V(|\Phi|)) , \quad (1)$$

where \dagger denotes complex conjugation, and $g_{\mu\nu}$ is the spacetime metric, determined by the Einstein equations. These gravitational solitons exhibit several interesting properties. Firstly, their masses and compactness can reach significantly higher values compared to their simpler mini-boson star cousins, arising from a potential consisting only of a mass term, $V = \mu^2|\Phi|^2$. Moreover, even when compared to quartic self-interacting boson stars [68], these Q -stars can be more compact (see [69] for a direct comparison). Their radius can be as small as their associated Schwarzschild light ring, as demonstrated in [70, 71], or can even approach the Schwarzschild radius when using an alternative definition of the radius [72].

Secondly, Q -stars have appealing stability properties. For example, the sequence of solutions can form two disconnected stable branches in both spherical [72, 73] and dipolar configurations [36]. Additionally, for rotating boson stars, certain stable regions—though not full branches—have been identified [38, 41], whereas mini-boson stars are unstable in the rotating case [37]. Finally, these boson star spacetimes have been shown to release energy and angular momentum when interacting with incident waves, meaning that they can participate in superradiant processes [39, 41, 44]. Q -stars are a class of dynamically robust compact objects capable of mimicking the observational appearance of a black hole. In particular, as discussed in the following sections, they can produce an effective shadow comparable in size to that of a black hole.

In [54], the observational appearance of a non-rotating mini-boson star was studied using GRMHD simulations followed by radiative transfer calculations. Two different boson star spacetimes were considered, with a key distinction in their background properties that ultimately influenced the simulations. Specifically, the angular velocity profile Ω for circular (timelike) geodesics exhibited an inner region where Ω decreased toward the center in one configuration, while no such region existed in the other. The presence of this inner region, where magnetorotational instability is suppressed (as will be discussed in the next section), was found to play a crucial role. In particular, the authors noticed that the location of the maximum of Ω coincided with the inner radius of a small torus of stalled plasma, leading to the formation of a dark region at the center of one of the horizonless and surfaceless object explored while for the other one, with monotonically decreasing profile of Ω , the plasma accumulated at the center.

We build upon the hypothesis proposed in [54] and conjecture that the existence of dark central regions surrounded by bright emission in black hole mimicker spacetimes depends on the presence of an inner region with Ω increasing as a function of the radius r . Moreover, we expect that the farther this maximum is from the center of the mimicker, the larger the resulting shadow will be. For mini-boson stars, only certain configurations within the unstable branch were found to exhibit an angular velocity profile Ω (cf. Eq. (5)) with a local maximum for $r > 0$. This raises the question of whether it is possible to obtain a stable configuration in a model that could also produce an expected shadow. To complete this two-fold task, we now explore Q -stars as a simple model capable of realizing this scenario. We find that a quartic term (λ) in the potential alone is insufficient; however, the interplay between the quartic and sextic terms allows for the construction of a successful configuration.

¹ This applies to the case of non-topological solitons in 3+1 dimensions within an effective field theory involving a single scalar field [3]. A model without higher dimensional effective operators can be easily written down when allowing for two scalar fields, as considered in the earlier work [2].

A. Families of Q -stars and the role of self-interactions

We begin by defining some convenient rescalings of the parameters λ and ν which can be derived from the rescaling of the full system by considering $1/\mu$ as a length and time unit. In particular, we use the same conventions as in [41]:

$$g = \frac{\lambda M_{\text{P}}^2}{\mu^2}, \quad h = \frac{\nu M_{\text{P}}^4}{\mu^2}, \quad (2)$$

defining new coordinates $\tilde{x}^a = x^a \mu$, the field $\tilde{\Phi} = \Phi/M_{\text{P}}$, where $M_{\text{P}} = 1/\sqrt{8\pi G}$ is the reduced Planck mass. After rescaling and removing the tilde symbols from \tilde{x}^a and $\tilde{\Phi}$ for simplicity, the equations of motion that determine Φ and $g_{\mu\nu}$ conform the Einstein-Klein-Gordon system and take the (dimensionless) form $G^\mu{}_\nu = 8\pi G T^\mu{}_\nu$ and $(\nabla^\kappa \nabla_\kappa - V')\Phi = 0$, where the energy momentum is given by Eq. (1), the scalar potential by

$$V(|\Phi|) = |\Phi|^2 + \frac{1}{2}g|\Phi|^4 + \frac{1}{3}h|\Phi|^6, \quad (3)$$

and we have defined $V' := dV/d|\Phi|^2 = 1 + g|\Phi|^2 + h|\Phi|^4$. The model has two independent parameters, g and h . With this in mind, we proceed to solve the Einstein-Klein-Gordon equations to find stationary solutions. To construct spherical static boson stars, we consider:

$$\Phi = \phi(r)e^{-i\omega t}, \quad ds^2 = -e^{2F_0(r)} dt^2 + e^{2F_1(r)} (dr^2 + r^2 d\Omega^2). \quad (4)$$

with ω a real number to be determined by the boundary conditions and corresponding to the frequency of pulsation of the scalar field. From the metric ansatz in (4), we see that the background is solved in the isotropic gauge.

We solve numerically for the functions ϕ , F_0 , F_1 and the unknown ω using the equations fully displayed in [41] and using the spectral code described in [74], splitting the r domain in 8 shells and using between 18 and 24 spectral coefficients. For each set of values (g, h) we construct sequences of solutions by varying the value² $F_0(0)$ starting from values $F_0(0) \rightarrow 0^-$, corresponding to the Newtonian limit. We calculate the value of the total mass M of the configurations by extracting it from the asymptotical behavior of the metric functions in Eq. (4). The radius R , often used to describe the size of a boson star, is defined as the areal radius enclosing 99% of the total mass. More precisely, in the coordinates given by (4), this radius is expressed as $R = e^{F_1(r_{99})} r_{99}$, where r_{99} is the (isotropic) radial coordinate r at which the Misner-Sharp mass function, $M(r) = -2r/(1 + r\partial_r \ln \Psi)$, satisfies $M(r_{99}) = 0.99M$. Both quantities, the mass and radius of some families of solutions of Q -stars are displayed in Fig. 1. In this figure and from this point onward, we will use units such that $G = 1$.

B. Selection of the configurations

To better understand the role of the parameters g and h in shaping the properties of the resulting boson stars, we begin by considering the Newtonian limit, where $\Phi \rightarrow 0$. This corresponds to the limits $M \rightarrow 0$, $\omega \rightarrow \mu$, and $R \rightarrow \infty$ in Fig. 1. In this regime, the influence of the higher-order interaction terms, parameterized by g and h , is negligible, and all families of solutions exhibit similar behavior as they approach this limit.

Next, we compare the mini-boson star case ($g = 0 = h$) with configurations that have either positive or negative values of g keeping the sextic term zero. When g is positive, corresponding to a repulsive self-interaction, the stars become more massive as g increases, with their mass scaling as a power of g [68]. However, their compactness and frequency profiles approach an asymptotic limit [68]. Notably, for positive g , the spiral structure in the M vs. ω diagram does not unroll indefinitely as g grows. Instead, all configurations remain confined within the range $0.8\mu \lesssim \omega < \mu$, as illustrated by the $g = +10$ gray curve in Fig. 1. An important aspect of these M vs. ω diagrams is that stable boson stars lie along stable branches, defined by regions where $dM/d\omega < 0$, extending from the Newtonian limit at $M \rightarrow 0$ to the global minimum of ω - see [75] for a generic discussion of perturbative stability of spherical bosonic stars. Quartic self-interacting boson stars possess only a single stable branch, as can be confirmed in the figure.

For negative g , the self-interaction becomes attractive, leading to less massive configurations [76] and causing the spiral to unroll. If $|g|$ is sufficiently big, such as the $g = -10$ gray curve in Fig. 1, the frequency can extend down to $\omega \rightarrow 0$. This behavior is represented using arrows in the left panel of Fig. 1. In addition to these effects, a negative

² Depending on the values (g, h) , sometimes $F_0(0)$ is not a good parameter to parametrize the sequence of solutions. For these cases we vary ω instead.

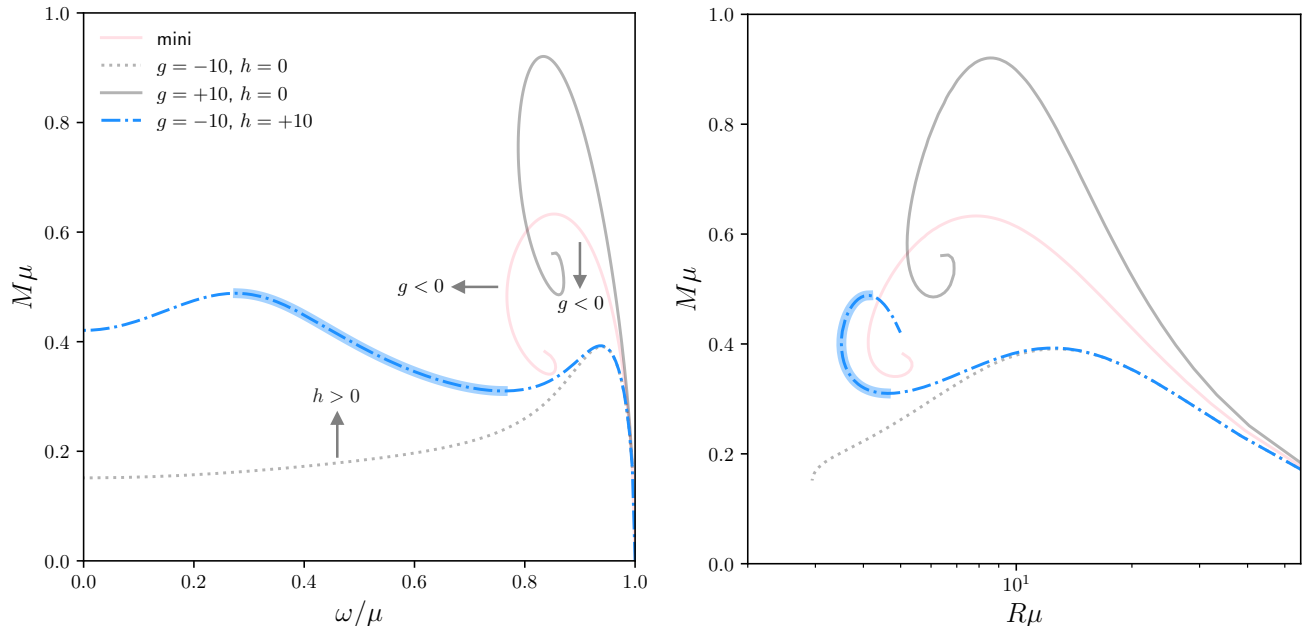


FIG. 1. Q -star sequences for different values of the self-interacting parameters g and h . We include for comparison the mini-boson star and show with arrows the effect of including a negative g (for positive g the behavior follows the opposite direction). Also with an arrow we indicate the effect of including a positive h in the strong field region in the sequences of negative g . The thick blue curve denotes the second stable region: the relativistic stable branch.

g shifts the maximum mass toward higher values of ω . When extending the solutions into the strong-field regime (large $|\Phi|$), introducing a positive value of h provokes additional repulsive interaction that becomes significant at larger $|\Phi|$, creating conditions for a second region of stability. This second stable region, referred to as the *relativistic stable branch*, is illustrated in Fig. 1 for the case $g = -10$ and $h = +10$ (thick blue curve). We have verified the stability of several configurations along this curve using full 3+1 numerical relativity, particularly for cases with $\omega/\mu = \{0.3, 0.4, 0.5, 0.6, 0.7\}$, employing the *Einstein Toolkit* [77] as implemented in [41].

As noted earlier, mini-boson stars exhibit a local maximum of the angular velocity Ω at $r > 0$ only in the unstable branch, meaning that configurations most relevant for mimicking a black hole reside deep within the “spiral” region of solutions where the location of the maximum is far away from the center. For the family of Q -stars with negative g and positive h , however, as mentioned above, the spiral unrolls, creating the relativistic stable branch. Furthermore, as shown in the right panel of Fig. 1, the masses in this relativistic stable branch remain comparable to those of other boson stars, but their radii R are significantly smaller, making these configurations more *compact*. This leads us to the question of effective shadow formation: are these stable configurations also likely to possess local maxima of Ω ?

The magnitude of the angular velocity, as measured at infinity, of a timelike circular orbit in the spacetime of a spherical Q -star represented by the metric (4) is³

$$\Omega(r) := \left| \frac{d\varphi}{dt} \right| = e^{F_0 - F_1} \left(\frac{F'_0}{r + r^2 F'_1} \right)^{1/2}. \quad (5)$$

Local maxima at $r > 0$ can be identified by evaluating the angular velocity profiles, Ω , for all solutions obtained for each set of parameters (g, h) . We denote the areal radius at which Ω reaches this turning point as r_{turn} . In the region inside r_{turn} , *i.e.* where $d\Omega/dr > 0$, the magnetorotational instability is suppressed [78]. In this way, using the metric coefficients, it is possible to estimate the presence of a region of luminosity depletion, even if the non-gravitational part of the central body does not interact with light, as is the case of a scalar star.

We first reproduce the known results for the location of this turning point in the case of a mini-boson star [54]. Our focus is then turned to the sequence of solutions with $g = -10$ and $h = +10$, confirming that a turning point indeed exists. Moreover, we find that a significant portion of this region (in this case, more than half) intersects with

³ See, *e.g.*, Eq. (8) of [55] applied to the metric (4).

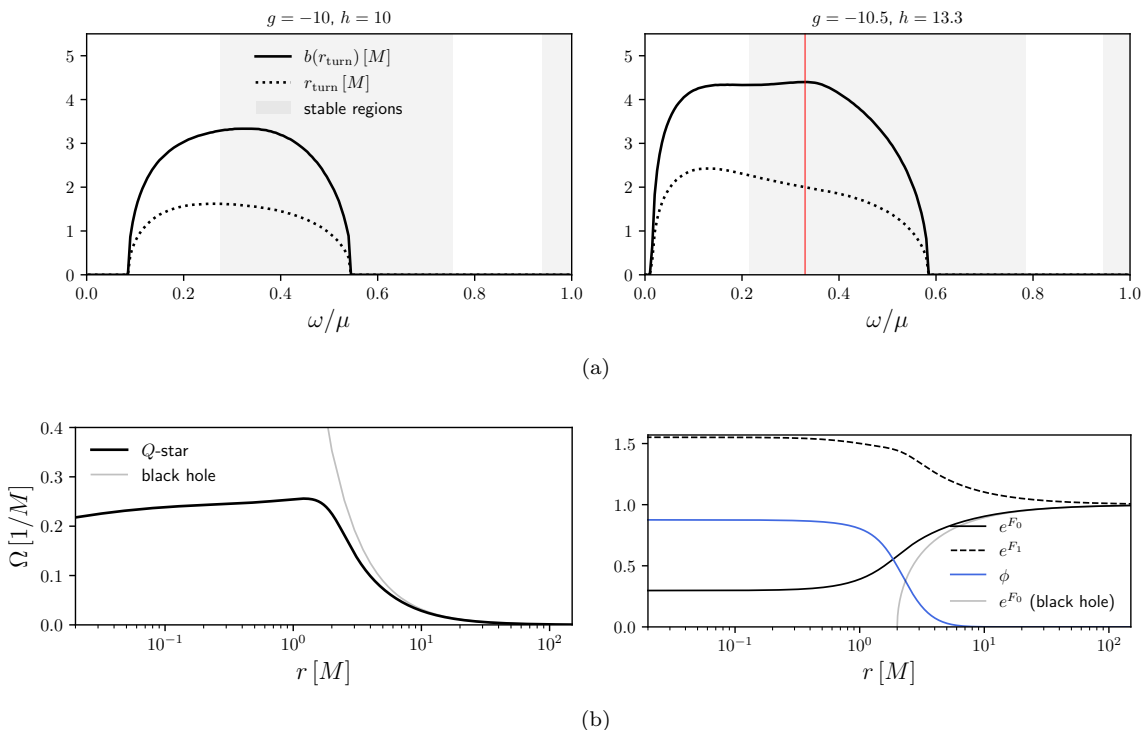


FIG. 2. Selection of the reference Q -star. Panel (a) shows the radius and impact parameter corresponding to the location of the local maximum in the angular frequency profile for two sequences of Q -stars. Notably, two stable regions emerge, corresponding to the stable branches of the background metric identified in Fig. 1. A thin red line marks the reference Q -star used in the GRMHD simulations. Panel (b) presents the angular velocity, metric functions, and scalar field profile for this reference Q -star, alongside comparisons with a Schwarzschild black hole. In this figure, $r[M]$ is not the radial coordinate (4), but the areal radius in units of M , *i.e.*, $r[M] := e^{F_1} r/M$.

the relativistic stable branch – see the left panel of Fig. 2 (a). Note that in this plot, we choose the total mass of the star, M , instead of μ , as the units for the dimensionless quantities such as r_{turn} .

The values of r_{turn} for this Q -star sequence with $g = -10$ and $h = +10$ are comparable to those found in unstable mini-boson stars, where a torus forms without penetrating the area with $d\Omega/dr > 0$. In such cases, ray-traced images revealed a dark region, although relatively smaller than that of a Kerr black hole [54]. An estimation of the expected size of such dark region is given by the impact parameter for a light ray grazing at r_{turn} , $b(r_{\text{turn}}) = r_{\text{turn}} e^{-F_0(r_{\text{turn}}) + F_1(r_{\text{turn}})}$. We find that both r_{turn} and the corresponding impact parameter $b(r_{\text{turn}})$ can be increased by exploring some close values of (g, h) . After a brief survey of a dozen solution families, we identify the sequence with $g = -10.5$, $h = 13.3$. In this case, the solution with $\omega = 0.33\mu$ attains a notably high impact parameter, $b(r_{\text{turn}}) = 4.4$ (see the right panel of Fig. 2). We designate this solution as our reference Q -star, characterized by $r_{\text{turn}} = 2.0$ with $\Omega = 0.081$, a total mass of $M = 0.624$, and compactness $M/R = 0.164$. The profiles of Ω , the metric functions, and the scalar field are shown in panel (b) of Fig. 2, along with a comparison to the corresponding Schwarzschild solution of identical mass. Also for comparison, note that the impact parameter of the light ring of the Schwarzschild black hole is $b = \sqrt{27}M \simeq 5.2M$.

We have seen that the configuration with $(g = -10, h = 10)$ has a relativistic stable branch. In Fig. 3, we explore the values of g and h around that point. For each pair of values, we identify the largest possible impact parameter by constructing spacetime configurations for several values of ω . We use a color code to indicate such largest value for each pair in Fig. 3. Notice that the plot seems to indicate a zone of (g, h) points with large impact parameters.

As mentioned, in presenting the results in Fig. 2 and Fig. 3, we have used M instead of μ as units to construct dimensionless quantities. This choice is particularly convenient when treating the Q -star as a black hole mimicker, as will be explored in the next section. To facilitate numerical simulations, we have prepared tabulated data for the background solution of our reference Q -star and interpolated it into the areal gauge, given by $ds^2 = -e^{2F_0} dt^2 + a^2 dr_a^2 + r_a^2 d\Omega^2$. These interpolated fields are then fed to the GRMHD code as functions of the dimensionless radius⁴

⁴ In the code we deal with the dimensionless radius μr and receive as one of the outputs the dimensionless mass μM . Therefore the

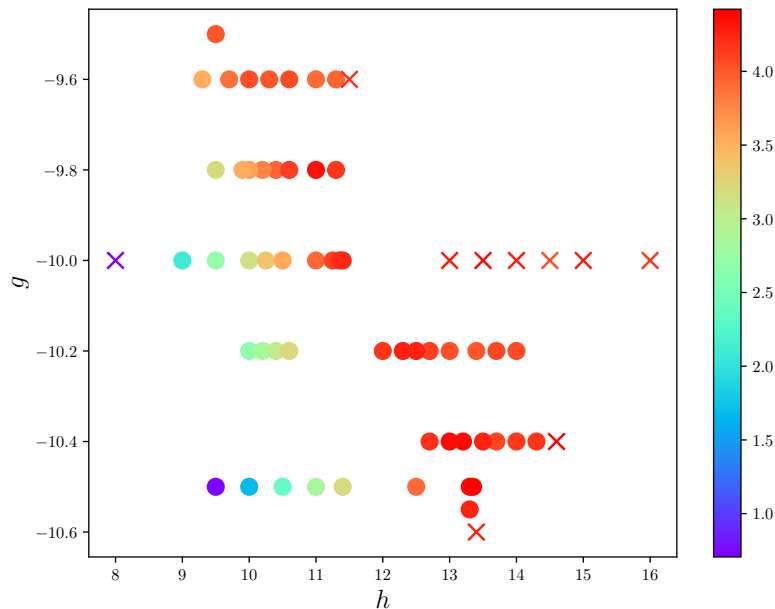


FIG. 3. Map plot for values of g and h with a relativistic stable region around $(g = -10, h = 12)$. Different colors are used to denote the largest values of the impact parameter $b(r_{\text{turn}})$ for the corresponding values of g and h . Crosses indicate that such values are not in the stable branch.

r_a/M . In the following section we will drop the a subindex and use r to represent the areal radius.

III. GENERAL RELATIVISTIC MAGNETOHYDRODYNAMIC SIMULATIONS

A. Simulation setup

As our spacetime background, we adopt the reference Q -star identified in the previous section, corresponding to the solution with $\omega = 0.33\mu$ and couplings $(g, h) = (-10.5, 13.3)$. This configuration lies on the relativistic stable branch and is distinguished by the large radius at which the angular velocity reaches its maximum, yielding a correspondingly large impact parameter. We perform a 3D simulation of magnetized accretion onto this reference Q -star. The simulation evolves the equations of GRMHD using the code BHAC (<https://bhac.science>, see [79, 80] for more details on the code and the formulation of the GRMHD equations used). As initial conditions, we use a torus with constant angular momentum $\ell = -u_\phi/u_t$ [81] such that its inner radius is at $r = 18 M$ and its density maximum is at $r = 25 M$, where r is the areal coordinate. We choose such a location for the torus to ensure that material arriving in the vicinity of the Q -star smoothly falls towards smaller radii due to the magneto-rotational instability (MRI) and no big transients are present. To trigger turbulence through the MRI, we set up a poloidal magnetic field loop described by the vector potential

$$A_\phi \propto \max(0, \rho/\rho_{\text{max}} - 0.2), \quad (6)$$

where ρ is the particle number density in the fluid frame and ρ_{max} is its maximum value in the initial torus, and perturb the solution by adding white noise with an amplitude of 4% to the pressure. The initial magnetic field is such that the ratio between the highest thermal pressure and the highest magnetic pressure in the torus is $p_{\text{max}}/p_{\text{mag,max}} = 1000$. The fluid obeys an ideal gas equation of state with adiabatic index $\hat{\gamma} = 4/3$. To emulate vacuum regions outside the torus, the rest of the domain is filled with a tenuous atmosphere following the profiles $\rho_{\text{atmo}} = \rho_{\text{min}}(r + r_0)^{-3/2}$

dimensionless radius can be expressed as $r_a/M = e^{F_1(\mu r)/(\mu M)}$.

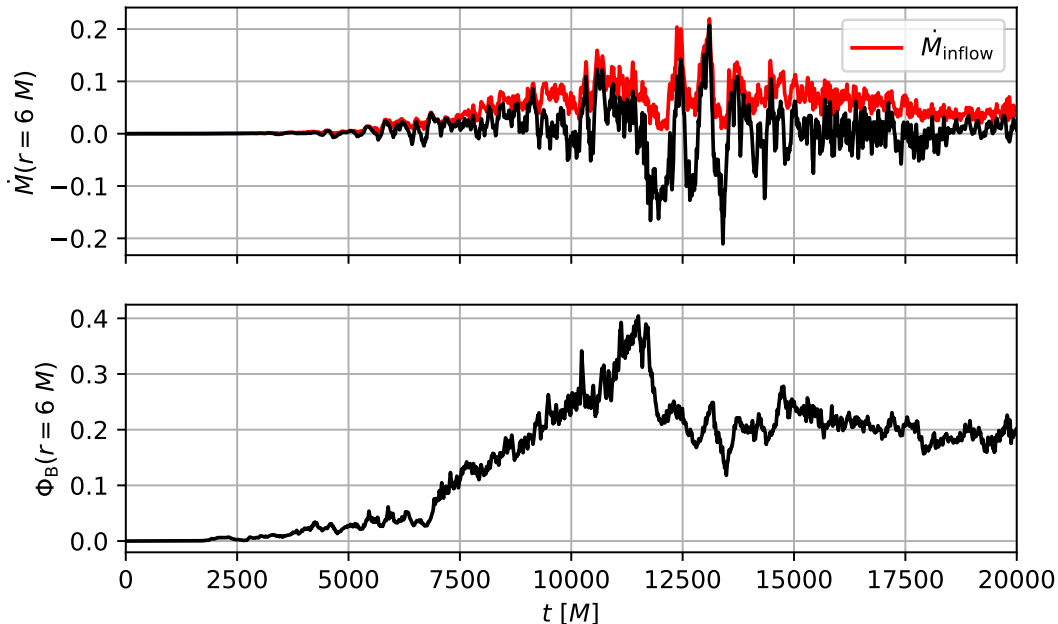


FIG. 4. Time series of the mass accretion rate \dot{M} and radial magnetic flux Φ_B through a spherical surface at $r = 6 M$.

and $p_{\text{atmo}} = p_{\text{min}}(r + r_0)^{-5/2}$, where $r_0 = 1 M$, $\rho_{\text{min}} = 10^{-5}\rho_{\text{max}}$ and $p_{\text{min}} = 10^{-7}p_{\text{max}}$. These profiles are also used to reset p and ρ whenever they fall below the atmosphere values during the course of the simulation. We also evolve a passive tracer ρ_{tr} that is advected with density. This tracer is initialized at $\rho_{\text{tr}} = 1$ inside the torus and at $\rho_{\text{tr}} = 0$ outside of it. We reset p and ρ to their atmosphere values whenever $\rho_{\text{tr}} < 0.1$ in order to prevent artificial accumulation of atmosphere material at the origin.

We employ a finite volume (FV) scheme with a total variation diminishing Lax-Friedrichs (TVDLF) Riemann solver (also known as Rusanov fluxes) with piecewise parabolic reconstruction (PPM) [82] and a simple two-step predictor-corrector time integration. To evolve magnetic fields while keeping the solenoidal constraint fulfilled, we employ the upwind constrained transport scheme of [83].

The simulation is performed in spherical coordinates, with the domain extending over $r/M \in [0, 2500]$. Internally, we employ a logarithmic radial coordinate s , related to the areal coordinate r by the transformation $r = \exp(s) - 1$. In order to ensure sufficient resolution of the MRI while avoiding small time steps near the origin due to the Courant-Friedrichs-Lewis (CFL) condition, we employ four levels of fixed mesh refinement. Cells in direct contact with the origin are kept at base resolution ($N_r \times N_\theta \times N_\phi = 64 \times 16 \times 16$), while parts of the domain at the highest refinement level are evolved at effective resolution of $512 \times 128 \times 128$.

B. Results

1. Simulation results

During the initial part of the simulation, the behavior shown is similar to that observed for black holes in the ‘Standard And Normal Evolution’ (SANE) regime: turbulence develops as a result of the MRI and material slowly falls into progressively smaller orbits [84]. However, different from the black hole case, instead of disappearing behind the event horizon, matter accumulates close to the center of the boson star. This accumulation initially does not occur at the center, but slightly away from it, forming a torus around the location predicted in the previous Sections. This is also similar to what was observed in [54] for mini-boson stars. Eventually, material diffuses to the empty space inside the ring, consistent with the numerical viscosity estimated for the grid resolution used. In the rest of this Section we provide a few diagnostics for a more quantitative description of the simulation behavior.

We quantify the mass accretion rate \dot{M} and the absolute value of the magnetic flux Φ_B through a spherical surface, defined as

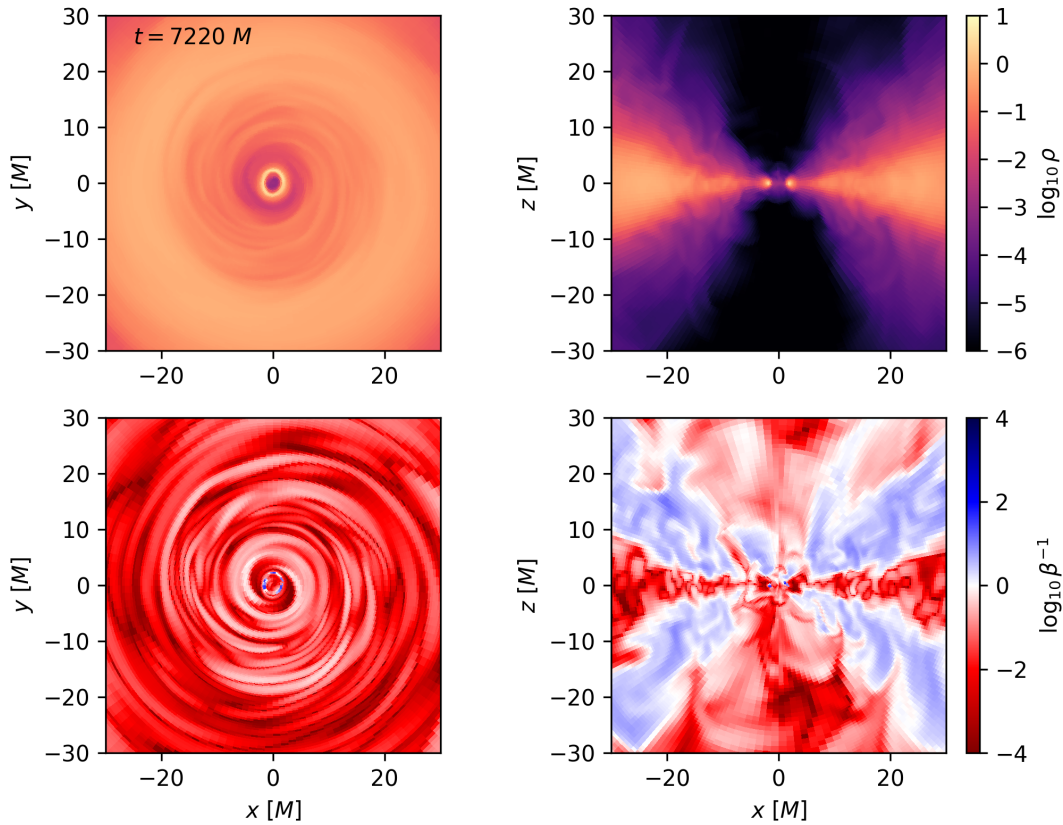


FIG. 5. Snapshot of the simulation at $t = 7220 M$, showing density in code units (*top panels*) and plasma beta magnetization $\beta := p_{\text{gas}}/p_{\text{mag}}$ (*bottom panels*) on the equatorial plane (*left panels*) and the meridional plane (*right panels*).

$$\dot{M}(r) := - \int_0^{2\pi} \int_0^\pi \rho u^r \sqrt{-g} d\theta d\phi, \quad (7)$$

$$\Phi_B(r) := \frac{1}{2} \int_0^{2\pi} \int_0^\pi |{}^*F^{rt}| \sqrt{-g} d\theta d\phi, \quad (8)$$

where u^r is the radial component of the fluid 4-velocity, ${}^*F^{\mu\nu}$ is the dual of Faraday's tensor, and g is the metric determinant.

Fig. 4 shows time series of these quantities through a spherical surface at $r = 6 M$. Matter starts accreting through that radius around $t/M = 2500$; however, while for BH simulations \dot{M} remains always positive, in our simulation it displays large oscillations around a small positive value. This behavior, similar to that observed in [54], indicates that only a small fraction of accreting matter actually accumulates inside in the region $r < 6 M$, while the rest of it escapes in the form of a barionic wind. To show this, we also plot in Fig. 4 the total mass inflow, calculated as

$$\dot{M}_{\text{inflow}}(r) := - \int_0^{2\pi} \int_0^\pi \rho \min(u^r, 0) \sqrt{-g} d\theta d\phi, \quad (9)$$

from which it can be seen that there is a steady inflow of matter even during the times in which the total mass accretion rate becomes negative.

The magnetic flux displays an initial increase, after which it becomes quasi-stationary around $t/M \sim 12000$. The usual definition of the 'MAD parameter' [85] $\phi_{\text{MAD}} := \Phi_B / \sqrt{\langle \dot{M} \rangle}$ at this quasi-stationary phase would classify the system within the MAD regime, $\phi_{\text{MAD}} \gtrsim 15$ (in Lorentz-Heaviside units, which we use in this work); however, the simulation does not show the magnetic flux eruptions that characterize the magnetically arrested disk (MAD) state. This indicates that the usual expression for the MAD parameter may not be adequate to classify systems with

important outflows that drive the mass accretion rate close to zero, as may happen in horizonless exotic compact objects.

We now analyze the morphology of the accretion flow using representative 2D slices. From $t \sim 7000$, density maps show the formation of a stalled torus near the predicted location of $r_{\text{turn}} = 2 M$. This torus shows noticeable oscillations due to epicyclic motion that distorts it into an elliptic shape (Fig. 5). However, it appears remarkably stable and survives with a significant density contrast for several thousands of M in time, until matter starts to diffuse to the central hollow region.

As a way to quantify the size of the hollow, we keep track of the location of the density maximum within the inner $2.5 M$. We calculate it by first obtaining the ϕ -averaged profile of ρ in the equatorial plane as⁵

$$\langle \rho \rangle(r) = \frac{1}{2\pi} \int_0^{2\pi} \rho(r, \theta = \pi/2, \phi) d\phi \quad (10)$$

and then finding the radial coordinate of the local density maximum ρ_{max} within $r < 2.5 M$, that we denote as $r(\rho_{\text{max}})$. The evolution of this quantity is shown in Fig. 6 over the full duration of the simulation. To reflect the discreteness of the numerical domain, each data entry is represented by a rectangle with a vertical size equivalent to the radial extension of the computational cell that contains the density maximum, and a horizontal size of $10 M$ (the output cadence). To quantify the relative importance of this maximum, we calculate the ratios $\delta\rho = \rho(r_{\text{max}})/\rho(r_{\text{O}})$ and $\delta j_{\text{sync}} = j_{\text{sync}}(r_{\text{max}})/j_{\text{sync}}(r_{\text{O}})$ of density and synchrotron emissivity j_{sync} between the location of the maximum (r_{max} and the cell closest to the coordinate origin r_{O}). Synchrotron emissivity is approximated as

$$j_{\text{sync}} \propto \rho \Theta_e^2 \exp \left[-0.2 (b \Theta_e^2)^{-1/3} \right] \quad (11)$$

which is valid for an optically thin plasma in the frequency band accessible to the EHT [86]. Here b is the strength of the magnetic field in the fluid frame, and $\Theta_e := k_{\text{B}}T/m_e c^2$ is the dimensionless temperature of electrons, which we assume to be the same as that of ions in our simulation. The ratio δj_{sync} is invariant with respect to changes in the density scale of the simulation, even if j_{sync} is not.

Before $t \sim 3 \times 10^3 M$, the local density maximum is located at the cell next to the origin. During this time, the accretion flow has not reached $r < 25 M$ and the local maxima reflect mainly the atmosphere prescription and numerical noise. Near $t \sim 3 \times 10^3 M$, matter starts accumulating close to the location expected from the Ω_{max} prediction. The local maximum then remains mostly within $\pm 0.5 M$ from the expected location until $t \sim 1.1 \times 10^4 M$. Deviations are indeed expected, as other mechanisms neglected by the Ω_{max} model are in play, such as pressure gradients, turbulent velocity fluctuations and numerical viscosity. Near $t \sim 1.1 \times 10^4 M$, the density maximum starts shifting slowly towards the origin. Between $t \sim 1.45 \times 10^4 M$ and $t \sim 1.65 \times 10^4 M$, it is possible to notice a competition between a local maximum near $r = 1.75 M$ formed by incoming matter and another one near $r = 0.75 M$ formed by matter that has been accumulating around the origin, until the inner maximum dominates ($t \sim 1.65 - 1.85 \times 10^4 M$), to then shift towards the origin near $t \sim 1.85 \times 10^4 M$, and remain there until the end of the simulation.

The evolution after $t \sim 1.1 \times 10^4 M$ can be understood from the fact that in addition to the MRI there are other mechanisms able to transport angular momentum, although with longer associated timescales.

2. Numerical viscosity and lifetime of the central hollow

The fact that the plasma eventually overcomes the centrifugal barrier and fills the hollow necessarily means that there are other processes in the simulation that transport angular momentum, although at a slower rate than the MRI. The longer viscous timescale associated with these processes prevented the filling of the hollow from being observed in [54], where the simulation was run for a shorter time. (For comparison, the simulation for boson star model A reported there lasted until $10000 M$, while in our simulation we observe matter penetrating the effective barrier around $17000 M$, c.f. Fig. 6). Due to the length of the simulation, it becomes relevant to estimate the timescale associated to numerical viscosity, which can produce the necessary angular momentum transport without any mechanism other than the MRI being present in the simulation. This does not exclude that such other processes are involved in the real system (e.g. molecular viscosity), although acting on much longer timescales. The viscous timescale τ is an estimation of the time required by viscosity ν to diffuse mass or momentum over a characteristic length L , and is given by

⁵ Due to the axial symmetry, we do not need to weight by the metric determinant.

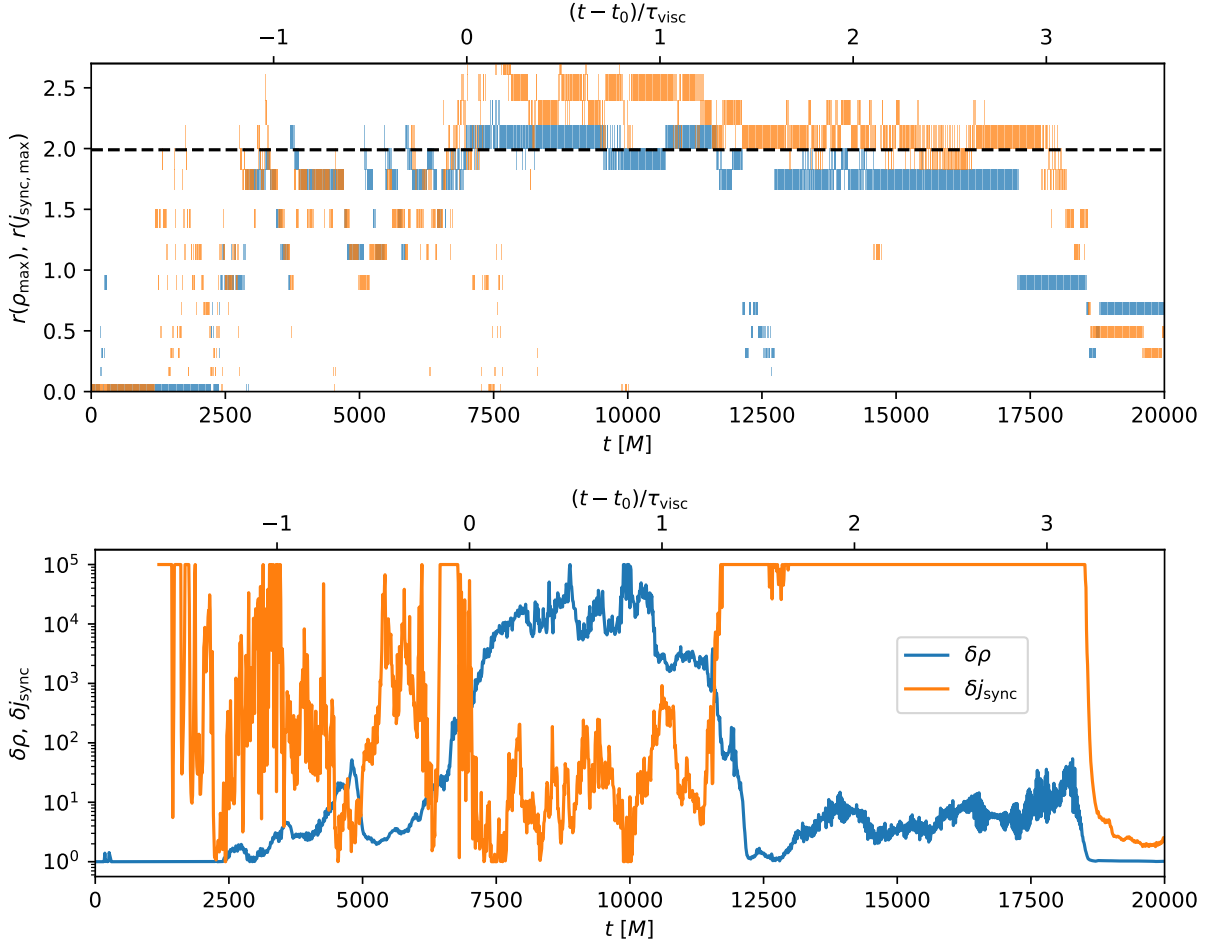


FIG. 6. Top panel: evolution of the location of the local maxima of density ρ and synchrotron luminosity proxy j_{sync} within $r < 2.5 M$. The prediction from the maximum Ω for circular geodesics ($r_{\text{max}} = 1.99 M$) is shown as a dashed line. The vertical length of each rectangle is the radial extension of the computational cell containing the maximum. Bottom panel: evolution of the density and the luminosity contrast between the local maximum and the cell closest to the origin. In both panels, the upper horizontal axis shows time in units of the estimated numerical viscosity timescale (c.f. eq. (12)).

$$\tau_\nu = \frac{L^2}{\nu} = \frac{L^2}{\ell_{\text{turb}} u_{\text{turb}}} \text{Re}, \quad (12)$$

where in the last equality viscosity has been rewritten in terms of the Reynolds number Re , the typical velocity associated to turbulence u_{turb} and the length scale at which energy is injected into the turbulent cascade ℓ_{turb} .

It has been shown [87] that Reynolds number associated to numerical viscosity can be estimated as

$$\text{Re} = \left[\frac{2\ell_{\text{turb}}}{N_{\text{Re}}} \frac{1}{\Delta x_p} \right]^{p_{\text{Re}}}, \quad (13)$$

where Δx_p is the grid resolution, N_{Re} is a constant given by simulations such that if ℓ_{turb} is resolved by N_{Re} cells, $\text{Re} = 1$. From numerical experiments, it has been found that $N_{\text{Re}} \approx 0.7 - 1.5$, and that p_{Re} is close to the theoretical value $4/3$ for subsonic turbulence [87]. We may perform an order-of-magnitude estimation of the timescale associated to numerical viscosity at $r = 2 M$ by considering both $\ell_{\text{turb}} = L = 2 M$. Although the grid is not uniform due to the logarithmic radial coordinate and the different AMR levels, cells have approximately a square aspect ratio with $\Delta x_p \approx 0.175 M$ at that location. For the typical velocity scale u_{turb} , we choose the relative velocity between circular geodesics at $r = 2 M$ and the value needed to co-rotate with circular geodesics near the origin, that is,

$u_{\text{turb}} = r\Delta\Omega_K = 0.018$, where $\Delta\Omega = \Omega_K(r=2) - \Omega_K(r \rightarrow 0)$. In fact, before the dynamics is dominated by diffusion, the rotation profile in the disk is well approximated by circular geodesics. Substituting these values into equations (13) and (12), we obtain $\text{Re} = 65$ and $\tau_\nu = 3604 M$, which is relevant for the duration of our simulation.

The upper horizontal axis in Fig. 6 shows time measured in viscous timescales from the time where the density contrast between the torus of stalled matter and the origin reaches 10^3 . It can be seen that this high density contrast survives nearly one viscous timescale, while the location of the maximum at the predicted location survives for a longer time. This is an indication that numerical viscosity may be indeed the process behind the filling of the central hollow, and that this viscous diffusion would occur on a much longer timescale in a real system in which the process is associated to physical dissipation.

To get a sense of these timescales, we can estimate that corresponding to molecular viscosity. Although it is well known that this type of viscosity results in timescales of the order of the age of the Universe when applied to explain accretion in systems extending over hundreds of astronomical units, it is conceivable that it may become important in diffusing matter and momentum across the last gap from r_{turn} to the origin after the MRI has driven accretion until that radius. Molecular viscosity can be approximated as $\nu_m = \alpha\lambda c_s$, where λ is the mean free path of molecules within the fluid, c_s is the sound speed, and α is a factor of order unity that depends on the composition of the fluid, and can be obtained in some cases from statistical mechanics calculations. After substituting this expression in eq. (12), and setting again $L = r_{\text{turn}}$, we obtain

$$\tau_\nu = 1.5 \times 10^4 \text{ years} \left(\frac{1}{\alpha}\right) \left(\frac{n}{10^{12} \text{ cm}^{-3}}\right) \left(\frac{\sigma_m}{10^{-15} \text{ cm}^{-3}}\right) \left(\frac{0.1c}{c_s}\right) \left(\frac{r_{\text{turn}}}{2r_g}\right)^2 \left(\frac{M}{4 \times 10^6 M_\odot}\right)^2, \quad (14)$$

where n is the particle number density and σ_m is the cross-section of molecular collisions. The numeric values shown in the factors in parentheses in eq. (14) are reasonable choices, albeit with a high degree of uncertainty. For σ_m , we give an order-of-magnitude estimation for proton-proton collisions in the plasma. For n , we choose a value much larger than those employed in one-zone models of Sgr A* ($\simeq 10^6 \text{ cm}^{-3}$ [88]) from the consideration that the region around r_{turn} is accumulating matter over time. A more accurate estimation is beyond the scope of this work, however, it should take into account the long-term evolution of mass accretion rate, outflows through barionic winds, as well as viscous transport itself. It is interesting to notice that, although for an object of the mass of Sgr A* the timescale to diffuse matter to the center is short in astrophysical terms, it is much longer than the time it takes to matter to fall to r_{turn} over a comparable distance from the region in which the MRI is active (\simeq a few minutes), which emphasizes the fact that r_{turn} will be a region of accumulation. Furthermore, the dependence of eq. (14) on n shows that as density increases in that region, the timescale to diffuse matter to the origin will also increase. It is also interesting to notice the quadratic scaling of τ_ν with the mass of the object, which can increase independently from the rest of physical parameters in eq. (14). This results in a timescale of the order of 10^8 years for M87*.

Finally, we briefly consider other ways in which matter could lose angular momentum matter to fall inside r_{turn} . Angular momentum could be transported outward through spiral shocks in the disks; however, these are absent in our simulation. Another possibility is that matter decelerates due to magnetic fields lines anchored in the disk, which transfer angular momentum to the wind as in the process described by Blandford and Payne [89]. This classic model corresponds to a stationary, self-similar Newtonian solution for a Keplerian, geometrically thin accretion disk, which limits its applicability to our case of interest. However, we may gain some qualitative insight from the dependence of the angular momentum transported by the wind on the magnetic field strength (Section 5 of [89]). The wind in our simulations appears weakly magnetized, with $\beta = p_{\text{gas}}/p_{\text{mag}} \gtrsim 0.1$, while we may expect that the density in the disk will keep increasing. As matter accumulates near r_{turn} , it will become increasingly hard for magnetic torques to decelerate the disk. The detailed evolution of angular momentum transport in the mini-torus will depend on the interplay of angular momentum flux carried by matter coming from the exterior regions in the disk, and that escaping through the wind. It is unclear whether this process would lead to filling the central hollow in an observationally relevant timescale, or would simply contribute to removing excess angular momentum from matter that reaches r_{turn} . A detailed study of this process would require proper analytic modeling, or long-term simulations reducing the effect of numerical viscosity. This uncertainty, leads to the interpretation of eq. (14) as an upper limit.

3. Observational considerations

In order to evaluate the possibilities of Q -stars acting as black hole mimickers, it is necessary not only to verify the stalling of matter at the predicted radius, but also the formation of a bright ring compatible to the expected size of that measured by the EHT Collaboration. The upper panel of Fig. 6 shows that the location of the maximum of our proxy for synchrotron emissivity (equation 11) coincides with the predicted radius during most of the simulation, and that the contrast with respect to the origin is generally high (bottom panel of Figure 6). Although a detailed analysis

on how this radius translates to the size of the bright ring in images would require to perform general relativistic radiative transfer (GRRT) simulations, we can obtain some insight from the difference between $b(r_{\text{turn}})$ and the size of the observed ring for the simulations reported in [54]. The simulation of boson star A in such work shows a similarly remarkable agreement between the inner edge of the accretion disk and the predicted r_{turn} , which results in an impact parameter for grazing photons of $b(r_{\text{turn}}) = 2.88 M$. The bright ring seen in such simulations has a radius of $3.62 M$ (edge on) and $3.24 M$ (face on), projected on the image plane. The radius of the bright ring is therefore 12% – 25% larger than the impact parameter of grazing photons. We may use this information to make a reasonable prediction for our case of interest. For the Q -star used in our simulation, $b(r_{\text{turn}}) = 4.4 M$. From the estimates of mass and distance assumed by the EHT Collaboration [88] for Sgr A*, $1 M$ in projected distance corresponds to an angular size of $5.03 \mu\text{as}$ on the observer’s sky. Using this conversion factor, the impact parameter of the grazing photons for a Q -star with the parameters of Sgr A* corresponds to an angular size of $22.1 \mu\text{as}$. Therefore, we may expect a bright ring of angular diameter $49 - 55.4 \mu\text{as}$, which can be compared to the $51.8 \pm 2.3 \mu\text{as}$ measured by the EHT Collaboration [90]. This heuristic analysis suggests that the size of the bright ring of these BH mimickers may be compatible with current observations

IV. DISCUSSION AND CONCLUSIONS

In this work we investigated whether stable Q -stars can act as viable black hole mimickers through the formation of effective shadow-like features. Our analysis combined a study of geodesic structure in self-interacting boson star spacetimes with three-dimensional GRMHD simulations of magnetized accretion flows.

A key result is the predictive power of the angular-velocity profile of timelike circular geodesics, Eq. (5), as a first diagnostic for the expected morphology of the accretion flow. In astrophysical environments, matter surrounding a compact object typically forms a disk whose motion is well approximated by circular trajectories. The radial behaviour of $\Omega(r)$ therefore provides a proxy for the rotational properties of the plasma and for the conditions under which the magnetorotational instability (MRI) operates. In particular, the presence of a local maximum of Ω at a nonzero radius implies an inner region where $d\Omega/dr > 0$, suppressing the MRI and favouring the formation of a stalled torus. Since synchrotron emission is sourced by magnetized rotating plasma, this mechanism naturally leads to a central luminosity depression.

Guided by this idea, we explored the parameter space of solitonic boson stars and identified families of Q -star solutions for which the angular-velocity profile develops such a turning point while remaining within a stable branch of the background solutions. In contrast with mini-boson stars - where similar behaviour typically occurs only in unstable configurations - we found that suitable combinations of quartic and sextic self-interactions allow for stable, relativistic configurations with sizable values of r_{turn} and of the corresponding impact parameter $b(r_{\text{turn}})$. These configurations are therefore promising candidates to mimic the appearance of a black hole shadow.

We then performed GRMHD simulations of accretion onto a representative stable Q -star for which MRI suppression was expected to be active. The simulations confirm the qualitative picture suggested by the geodesic analysis. Matter transported inward by MRI-driven turbulence accumulates near the predicted location of r_{turn} , forming a long-lived toroidal structure with a pronounced density and emissivity contrast relative to the central region. This configuration produces a low-density, low-luminosity core consistent with an effective shadow, demonstrating that stable bosonic stars can participate in the “imitation game” without requiring ultracompactness or an ad hoc disk prescription.

At later times, the simulations reveal additional dynamical effects. Although the MRI is suppressed in the inner region, other mechanisms —such as turbulent transport and *numerical* viscosity— enable angular momentum redistribution on longer timescales, allowing matter to slowly diffuse toward the center. In our simulations, this process eventually fills the hollow region, suggesting that the effective shadow produced by the stalled torus might not be absolutely stable but instead is a long-lived feature. It is worth emphasizing that in realistic astrophysical systems the physical viscosity is far smaller than the numerical viscosity, so this quasi-stable state could persist for significantly longer timescales.

Interestingly, the simulations also hint at a secondary mechanism capable of producing central brightness depressions. Even when the inner region becomes partially filled with matter, the magnetic field configuration can retain a spiral morphology and remain displaced from the center, generating a ring-like emission pattern through synchrotron radiation. The detailed physical origin and robustness of this mechanism require further investigation, but it may provide an additional pathway for horizonless compact objects to produce shadow-like images.

Overall, our results provide a proof of principle that stable Q -stars can mimic key observational features commonly associated with black holes. The effective shadows obtained here are somewhat smaller than those of a Schwarzschild black hole of the same mass, but arise from a qualitatively different mechanism that does not rely on the presence of a light ring or extreme compactness. This strengthens the case for considering self-gravitating scalar configurations as viable alternatives in the interpretation of horizon-scale observations.

Several directions for future work remain open. A systematic exploration of the (g, h) parameter space could identify configurations yielding larger impact parameters and more pronounced effective shadows. Extending the analysis to rotating Q -stars is particularly important, given the relevance of spin for astrophysical sources. Incorporating radiative transfer calculations and producing synthetic images will allow for a more direct comparison with EHT observations. Finally, a deeper understanding of angular momentum transport in horizonless compact objects —both physical and numerical— will be essential to assess the longevity and observational relevance of the central brightness depressions reported here.

These developments will help clarify the extent to which horizonless compact objects can reproduce black hole-like phenomenology and, conversely, which observables may ultimately discriminate between the two scenarios.

ACKNOWLEDGMENTS

VJ acknowledges support from the National Key R&D Program of China under grant No. 2022YFC2204603. HO is supported by the Individual CEEC program - 5th edition funded by the Portuguese Foundation for Science and Technology (FCT). SYZ acknowledges support from the National Natural Science Foundation of China under grant No. 12475074 and No. 12247103. DN acknowledge the sabbatical support given by the Programa de Apoyos para la Superación del Personal Académico de la Dirección General de Asuntos del Personal Académico de la Universidad Nacional Autónoma de México in the initial stages of the present work. Simulations were performed on Mare Nostrum 5 under the FCT Advanced Computing Project 2024.07059.CPCA.A3 (<https://doi.org/10.54499/2024.07059.CPCA.A3>). This work was partially supported by the CONACyT Network Project No. 376127 “Sombras, lentes y ondas gravitatorias generadas por objetos compactos astrofísicos”, and also by the Center for Research and Development in Mathematics and Applications (CIDMA) (<https://ror.org/05pm2mw36>) under the Portuguese Foundation for Science and Technology (FCT, <https://ror.org/00snfq58>), Grants UID/04106/2025 (<https://doi.org/10.54499/UID/04106/2025>) and UID/PRR/04106/2025 (<https://doi.org/10.54499/UID/PRR/04106/2025>), and by the FCT projects 2022.04560.PTDC (with DOI <https://doi.org/10.54499/2022.04560.PTDC>), as well as 2024.05617.CERN (with DOI <https://doi.org/10.54499/2024.05617.CERN>). This work has further been supported by the European Horizon Europe staff exchange (SE) programme HORIZON-MSCA-2021-SE-01 Grant No. NewFunFiCO-101086251.

Appendix A: Central brightness depression in the final state

In the final stages of the simulation, we observe that the central region becomes filled with matter. Although the timescale at which this happens is consistent with that of numerical viscosity associated to the discretization, it can be expected that this behavior will occur in the long run due to slower physical diffusion processes. For this reason, it is interesting to describe the final state of our simulation. Fig. 7 shows this last snapshot for several quantities. It can be seen that density and pressure have reached nearly spherically-symmetric profiles. In contrast, the magnetic field has become ‘frozen’ in a spiral configuration with the maximum displaced with respect to the center. As synchrotron emissivity is proportional to the strength of the magnetic field (c.f. eq. (11)), this configuration produces the ring-like emission pattern that can be seen in the bottom right panel of the same figure.

At this stage, the MRI is inactive and Reynolds stress is negligible, as angular momentum has diffused and the rotation profile is nearly flat. The magnetic field is small (magnetic pressure is much smaller than gas pressure) and effectively, it is advected passively, rotating together with the central structure. In the long run, numerical or physical resistivity are expected to diffuse it away, producing a more uniform configuration. Nevertheless, it is interesting to notice that this is a relatively long-lived state that produces a ring-like structure in luminosity, even though the central structure has a nearly spherically symmetric distribution in density. This constitutes a possibility of producing ring-like images that, to our knowledge, has not been considered in the literature on exotic compact objects.

-
- [1] N. S. Manton and P. Sutcliffe, *Topological solitons*, Cambridge Monographs on Mathematical Physics (Cambridge University Press, 2004).
 - [2] R. Friedberg, T. D. Lee, and A. Sirlin, “A Class of Scalar-Field Soliton Solutions in Three Space Dimensions,” *Phys. Rev. D* **13**, 2739–2761 (1976).
 - [3] Sidney R. Coleman, “Q-balls,” *Nucl. Phys. B* **262**, 263 (1985), [Addendum: *Nucl.Phys.B* 269, 744 (1986)].
 - [4] Gerald Rosen, “Particlelike Solutions to Nonlinear Complex Scalar Field Theories with Positive-Definite Energy Densities,” *J. Math. Phys.* **9**, 996 (1968).

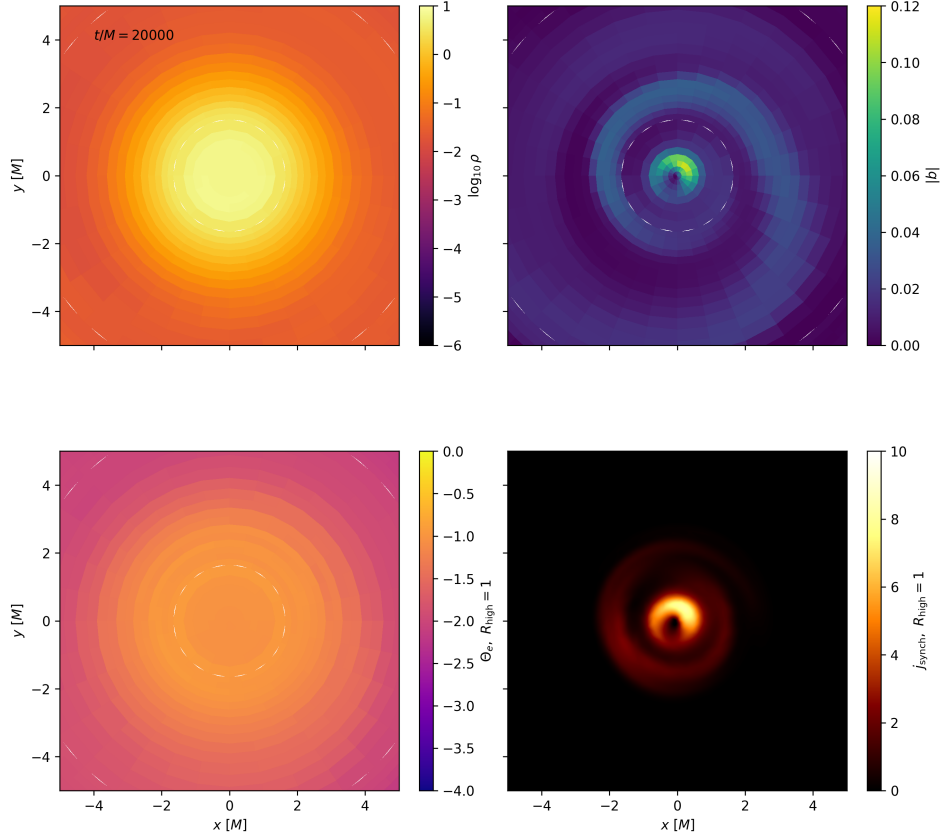


FIG. 7. Snapshot of the simulation at $t = 20000 M$.

- [5] Shuang-Yong Zhou, “Non-topological solitons and quasi-solitons,” Rept. Prog. Phys. **88**, 046901 (2025), arXiv:2411.16604 [hep-th].
- [6] Alexander Kusenko, “Solitons in the supersymmetric extensions of the standard model,” Phys. Lett. B **405**, 108 (1997), arXiv:hep-ph/9704273.
- [7] M. Laine and Mikhail E. Shaposhnikov, “Thermodynamics of nontopological solitons,” Nucl. Phys. B **532**, 376–404 (1998), arXiv:hep-ph/9804237.
- [8] Kari Enqvist, Asko Jokinen, and John McDonald, “Flat direction condensate instabilities in the MSSM,” Phys. Lett. B **483**, 191–195 (2000), arXiv:hep-ph/0004050.
- [9] Ian Affleck and Michael Dine, “A New Mechanism for Baryogenesis,” Nucl. Phys. B **249**, 361–380 (1985).
- [10] Kari Enqvist and John McDonald, “Q balls and baryogenesis in the MSSM,” Phys. Lett. B **425**, 309–321 (1998), arXiv:hep-ph/9711514.
- [11] Kari Enqvist and John McDonald, “B - ball baryogenesis and the baryon to dark matter ratio,” Nucl. Phys. B **538**, 321–350 (1999), arXiv:hep-ph/9803380.
- [12] Kari Enqvist and John McDonald, “The dynamics of Affleck-Dine condensate collapse,” Nucl. Phys. B **570**, 407–422 (2000), [Erratum: Nucl.Phys.B 582, 763–763 (2000)], arXiv:hep-ph/9908316.
- [13] S. Kasuya and M. Kawasaki, “Q Ball formation in the gravity mediated SUSY breaking scenario,” Phys. Rev. D **62**, 023512 (2000), arXiv:hep-ph/0002285.
- [14] Tuomas Multamaki and Iiro Vilja, “Simulations of Q ball formation,” Phys. Lett. B **535**, 170–176 (2002), arXiv:hep-ph/0203195.
- [15] Keisuke Harigaya, Ayuki Kamada, Masahiro Kawasaki, Kyohei Mukaida, and Masaki Yamada, “Affleck-Dine Baryogenesis and Dark Matter Production after High-scale Inflation,” Phys. Rev. D **90**, 043510 (2014), arXiv:1404.3138 [hep-ph].
- [16] Alexander Kusenko and Mikhail E. Shaposhnikov, “Supersymmetric Q balls as dark matter,” Phys. Lett. B **418**, 46–54 (1998), arXiv:hep-ph/9709492.
- [17] Kari Enqvist and John McDonald, “MSSM dark matter constraints and decaying B balls,” Phys. Lett. B **440**, 59–65 (1998), arXiv:hep-ph/9807269.
- [18] Robi Banerjee and Karsten Jedamzik, “On B-ball dark matter and baryogenesis,” Phys. Lett. B **484**, 278–282 (2000), arXiv:hep-ph/0005031.
- [19] Alexander Kusenko and Paul J. Steinhardt, “Q ball candidates for selfinteracting dark matter,” Phys. Rev. Lett. **87**, 141301 (2001), arXiv:astro-ph/0106008.

- [20] Leszek Roszkowski and Osamu Seto, “Axino dark matter from Q-balls in Affleck-Dine baryogenesis and the Omega(b) - Omega(DM) coincidence problem,” *Phys. Rev. Lett.* **98**, 161304 (2007), arXiv:hep-ph/0608013.
- [21] Ian M. Shoemaker and Alexander Kusenko, “Gravitino dark matter from Q-ball decays,” *Phys. Rev. D* **80**, 075021 (2009), arXiv:0909.3334 [hep-ph].
- [22] Shinta Kasuya and Masahiro Kawasaki, “Gravitino dark matter and baryon asymmetry from Q-ball decay in gauge mediation,” *Phys. Rev. D* **84**, 123528 (2011), arXiv:1107.0403 [hep-ph].
- [23] Shinta Kasuya, Masahiro Kawasaki, and Masaki Yamada, “Revisiting the gravitino dark matter and baryon asymmetry from Q-ball decay in gauge mediation,” *Phys. Lett. B* **726**, 1–7 (2013), arXiv:1211.4743 [hep-ph].
- [24] Masahiro Kawasaki and Hiromasa Nakatsuka, “Q-ball decay through A-term in the gauge-mediated SUSY breaking scenario,” *JCAP* **04**, 017 (2020), arXiv:1912.06993 [hep-ph].
- [25] David J. Kaup, “Klein-Gordon Geon,” *Phys. Rev.* **172**, 1331–1342 (1968).
- [26] Remo Ruffini and Silvano Bonazzola, “Systems of selfgravitating particles in general relativity and the concept of an equation of state,” *Phys. Rev.* **187**, 1767–1783 (1969).
- [27] Marcelo Gleiser and Richard Watkins, “Gravitational Stability of Scalar Matter,” *Nucl. Phys. B* **319**, 733–746 (1989).
- [28] Edward Seidel and Wai-Mo Suen, “Dynamical Evolution of Boson Stars. 1. Perturbing the Ground State,” *Phys. Rev. D* **42**, 384–403 (1990).
- [29] R. Friedberg, T. D. Lee, and Y. Pang, “Scalar Soliton Stars and Black Holes,” *Phys. Rev. D* **35**, 3658 (1987).
- [30] T. D. Lee, “Soliton Stars and the Critical Masses of Black Holes,” *Phys. Rev. D* **35**, 3637 (1987).
- [31] C. A. R. Herdeiro, J. Kunz, I. Perapechka, E. Radu, and Y. Shnir, “Chains of Boson Stars,” *Phys. Rev. D* **103**, 065009 (2021), arXiv:2101.06442 [gr-qc].
- [32] Romain Gervalle, “Chains of rotating boson stars,” *Phys. Rev. D* **105**, 124052 (2022), arXiv:2206.03982 [gr-qc].
- [33] Carlos A. R. Herdeiro and Eugen Radu, “Two Schwarzschild-like black holes balanced by their scalar hair,” *Phys. Rev. D* **107**, 064044 (2023), arXiv:2302.00016 [gr-qc].
- [34] Burkhard Kleihaus, Jutta Kunz, and Meike List, “Rotating boson stars and Q-balls,” *Phys. Rev. D* **72**, 064002 (2005), arXiv:gr-qc/0505143.
- [35] Víctor Jaramillo, Darío Núñez, Milton Ruiz, and Miguel Zilhão, “Full 3D nonlinear dynamics of charged and magnetized boson stars,” *Phys. Rev. D* **111**, 024070 (2025), arXiv:2411.07284 [gr-qc].
- [36] Pedro Ildefonso, Miguel Zilhão, Carlos Herdeiro, Eugen Radu, and Nuno M. Santos, “Self-interacting dipolar boson stars and their dynamics,” *Phys. Rev. D* **108**, 064011 (2023), arXiv:2307.00044 [gr-qc].
- [37] Fabrizio Di Giovanni, Nicolas Sanchis-Gual, Pablo Cerdá-Durán, Miguel Zilhão, Carlos Herdeiro, José A. Font, and Eugen Radu, “Dynamical bar-mode instability in spinning bosonic stars,” *Phys. Rev. D* **102**, 124009 (2020), arXiv:2010.05845 [gr-qc].
- [38] Nils Siemonsen and William E. East, “Stability of rotating scalar boson stars with nonlinear interactions,” *Phys. Rev. D* **103**, 044022 (2021), arXiv:2011.08247 [gr-qc].
- [39] Paul M. Saffin, Qi-Xin Xie, and Shuang-Yong Zhou, “Q-ball Superradiance,” *Phys. Rev. Lett.* **131**, 111601 (2023), arXiv:2212.03269 [hep-th].
- [40] Vitor Cardoso, Rodrigo Vicente, and Zhen Zhong, “Energy Extraction from Q-balls and Other Fundamental Solitons,” *Phys. Rev. Lett.* **131**, 111602 (2023), arXiv:2307.13734 [hep-th].
- [41] Fu-Ming Chang, He-Yu Gao, Víctor Jaramillo, Xin Meng, and Shuang-Yong Zhou, “Boson star superradiance with spinning effects and in time domain,” *Phys. Rev. D* **111**, 044053 (2025), arXiv:2412.01894 [gr-qc].
- [42] Guo-Dong Zhang, Cheng-Hao Li, Qi-Xin Xie, and Shuang-Yong Zhou, “Superradiance of Friedberg-Lee-Sirlin solitons,” *Phys. Rev. D* **111**, 103027 (2025), arXiv:2503.04657 [hep-th].
- [43] Guo-Dong Zhang, Shuang-Yong Zhou, and Meng-Fan Zhu, “Q-ball superradiance: Analytical approach,” (2025), arXiv:2510.27064 [hep-th].
- [44] He-Yu Gao, Paul M. Saffin, Yi-Jie Wang, Qi-Xin Xie, and Shuang-Yong Zhou, “Boson star superradiance,” *Sci. China Phys. Mech. Astron.* **67**, 260413 (2024), arXiv:2306.01868 [gr-qc].
- [45] Edmund J. Copeland, Paul M. Saffin, and Shuang-Yong Zhou, “Charge-Swapping Q-balls,” *Phys. Rev. Lett.* **113**, 231603 (2014), arXiv:1409.3232 [hep-th].
- [46] Qi-Xin Xie, Paul M. Saffin, and Shuang-Yong Zhou, “Charge-Swapping Q-balls and Their Lifetimes,” *JHEP* **07**, 062 (2021), arXiv:2101.06988 [hep-th].
- [47] Qi-Xin Xie, Paul M. Saffin, Anders Tranberg, and Shuang-Yong Zhou, “Quantum corrected Q-ball dynamics,” *JHEP* **01**, 165 (2024), arXiv:2312.01139 [hep-th].
- [48] Víctor Jaramillo and Shuang-Yong Zhou, “Complex structures of boson stars and anisotropic distribution of satellite galaxies,” *Phys. Rev. D* **110**, 084069 (2024), arXiv:2407.12084 [gr-qc].
- [49] Víctor Jaramillo and Shuang-Yong Zhou, “Dipoles and chains of solitons in the Friedberg-Lee-Sirlin model,” *Phys. Rev. D* **111**, 024027 (2025), arXiv:2411.08985 [gr-qc].
- [50] Pedro V. P. Cunha, Carlos A. R. Herdeiro, Eugen Radu, and Helgi F. Runarsson, “Shadows of Kerr black holes with scalar hair,” *Phys. Rev. Lett.* **115**, 211102 (2015), arXiv:1509.00021 [gr-qc].
- [51] P. V. P. Cunha, J. Grover, C. Herdeiro, E. Radu, H. Runarsson, and A. Wittig, “Chaotic lensing around boson stars and Kerr black holes with scalar hair,” *Phys. Rev. D* **94**, 104023 (2016), arXiv:1609.01340 [gr-qc].
- [52] Pedro V. P. Cunha, José A. Font, Carlos Herdeiro, Eugen Radu, Nicolas Sanchis-Gual, and Miguel Zilhão, “Lensing and dynamics of ultracompact bosonic stars,” *Phys. Rev. D* **96**, 104040 (2017), arXiv:1709.06118 [gr-qc].
- [53] Carlos A. R. Herdeiro, Alexandre M. Pombo, Eugen Radu, Pedro V. P. Cunha, and Nicolas Sanchis-Gual, “The imitation game: Proca stars that can mimic the Schwarzschild shadow,” *JCAP* **04**, 051 (2021), arXiv:2102.01703 [gr-qc].

- [54] Hector Olivares, Ziri Younsi, Christian M. Fromm, Mariafelicia De Laurentis, Oliver Porth, Yosuke Mizuno, Heino Falcke, Michael Kramer, and Luciano Rezzolla, “How to tell an accreting boson star from a black hole,” *Mon. Not. Roy. Astron. Soc.* **497**, 521–535 (2020), arXiv:1809.08682 [gr-qc].
- [55] Ivo Sengo, Pedro V. P. Cunha, Carlos A. R. Herdeiro, and Eugen Radu, “The imitation game reloaded: effective shadows of dynamically robust spinning Proca stars,” *JCAP* **05**, 054 (2024), arXiv:2402.14919 [gr-qc].
- [56] João Luís Rosa and Diego Rubiera-Garcia, “Shadows of boson and Proca stars with thin accretion disks,” *Phys. Rev. D* **106**, 084004 (2022), arXiv:2204.12949 [gr-qc].
- [57] João Luís Rosa, Caio F. B. Macedo, and Diego Rubiera-Garcia, “Imaging compact boson stars with hot spots and thin accretion disks,” *Phys. Rev. D* **108**, 044021 (2023), arXiv:2303.17296 [gr-qc].
- [58] Carlos A. R. Herdeiro and Eugen Radu, “Kerr black holes with scalar hair,” *Phys. Rev. Lett.* **112**, 221101 (2014), arXiv:1403.2757 [gr-qc].
- [59] Carlos Herdeiro, Eugen Radu, and Helgi Rúnarsson, “Kerr black holes with Proca hair,” *Class. Quant. Grav.* **33**, 154001 (2016), arXiv:1603.02687 [gr-qc].
- [60] Richard Brito, Vitor Cardoso, Carlos A. R. Herdeiro, and Eugen Radu, “Proca stars: Gravitating Bose–Einstein condensates of massive spin 1 particles,” *Phys. Lett. B* **752**, 291–295 (2016), arXiv:1508.05395 [gr-qc].
- [61] Joe Keir, “Slowly decaying waves on spherically symmetric spacetimes and ultracompact neutron stars,” *Class. Quant. Grav.* **33**, 135009 (2016), arXiv:1404.7036 [gr-qc].
- [62] Vitor Cardoso, Luís C. B. Crispino, Caio F. B. Macedo, Hirotada Okawa, and Paolo Pani, “Light rings as observational evidence for event horizons: long-lived modes, ergoregions and nonlinear instabilities of ultracompact objects,” *Phys. Rev. D* **90**, 044069 (2014), arXiv:1406.5510 [gr-qc].
- [63] Pedro V. P. Cunha, Carlos Herdeiro, Eugen Radu, and Nicolas Sanchis-Gual, “Exotic Compact Objects and the Fate of the Light-Ring Instability,” *Phys. Rev. Lett.* **130**, 061401 (2023), arXiv:2207.13713 [gr-qc].
- [64] Gabriele Benomio, Alejandro Cárdenas-Avenidaño, Frans Pretorius, and Andrew Sullivan, “Turbulence for spacetimes with stable trapping,” *Phys. Rev. D* **111**, 104037 (2025), arXiv:2411.17445 [gr-qc].
- [65] Gareth Arturo Marks, Seppe J. Staelens, Tamara Evstafyeva, and Ulrich Sperhake, “Long-Term Stable Nonlinear Evolutions of Ultracompact Black-Hole Mimickers,” *Phys. Rev. Lett.* **135**, 131402 (2025), arXiv:2504.17775 [gr-qc].
- [66] Tamara Evstafyeva, Nils Siemonsen, and William E. East, “Assessing the stability of ultracompact spinning boson stars with nonlinear evolutions,” *Phys. Rev. D* **113**, 044024 (2026), arXiv:2508.11527 [gr-qc].
- [67] Pedro V. P. Cunha, “Backreaction of perturbations around a stable light ring,” *JCAP* **05**, 083 (2025), arXiv:2503.00117 [gr-qc].
- [68] M. Colpi, S. L. Shapiro, and I. Wasserman, “Boson Stars: Gravitational Equilibria of Selfinteracting Scalar Fields,” *Phys. Rev. Lett.* **57**, 2485–2488 (1986).
- [69] Pau Amaro-Seoane, Juan Barranco, Argelia Bernal, and Luciano Rezzolla, “Constraining scalar fields with stellar kinematics and collisional dark matter,” *JCAP* **11**, 002 (2010), arXiv:1009.0019 [astro-ph.CO].
- [70] Michael Kesden, Jonathan Gair, and Marc Kamionkowski, “Gravitational-wave signature of an inspiral into a supermassive horizonless object,” *Phys. Rev. D* **71**, 044015 (2005), arXiv:astro-ph/0411478.
- [71] Caio F. B. Macedo, Paolo Pani, Vitor Cardoso, and Luís C. B. Crispino, “Astrophysical signatures of boson stars: quasinormal modes and inspiral resonances,” *Phys. Rev. D* **88**, 064046 (2013), arXiv:1307.4812 [gr-qc].
- [72] Burkhard Kleihaus, Jutta Kunz, and Stefanie Schneider, “Stable Phases of Boson Stars,” *Phys. Rev. D* **85**, 024045 (2012), arXiv:1109.5858 [gr-qc].
- [73] Fjodor V. Kusmartsev, Eckehard W. Mielke, and Franz E. Schunck, “Gravitational stability of boson stars,” *Phys. Rev. D* **43**, 3895–3901 (1991), arXiv:0810.0696 [astro-ph].
- [74] Miguel Alcubierre, Juan Barranco, Argelia Bernal, Juan Carlos Degollado, Alberto Diez-Tejedor, Víctor Jaramillo, Miguel Megevand, Darío Núñez, and Olivier Sarbach, “Extreme ℓ -boson stars,” *Class. Quant. Grav.* **39**, 094001 (2022), arXiv:2112.04529 [gr-qc].
- [75] Nuno M. Santos, Carolina L. Benone, and Carlos A. R. Herdeiro, “Radial stability of spherical bosonic stars and critical points,” *JCAP* **06**, 068 (2024), arXiv:2404.07257 [gr-qc].
- [76] J. Barranco and A. Bernal, “Self-gravitating system made of axions,” *Phys. Rev. D* **83**, 043525 (2011), arXiv:1001.1769 [astro-ph.CO].
- [77] EinsteinToolkit, “Einstein Toolkit: Open software for relativistic astrophysics,” <http://einstein toolkit.org/> (2025).
- [78] Steven A. Balbus and John F. Hawley, “A powerful local shear instability in weakly magnetized disks. 1. Linear analysis. 2. Nonlinear evolution,” *Astrophys. J.* **376**, 214–233 (1991).
- [79] Oliver Porth, Hector Olivares, Yosuke Mizuno, Ziri Younsi, Luciano Rezzolla, Monika Moscibrodzka, Heino Falcke, and Michael Kramer, “The Black Hole Accretion Code,” *Computational Astrophysics and Cosmology* **4**, 1 (2017), arXiv:1611.09720 Publisher: Springer International Publishing.
- [80] Hector Olivares, Oliver Porth, Jordy Davelaar, Elias R. Most, Christian M. Fromm, Yosuke Mizuno, Ziri Younsi, and Luciano Rezzolla, “Constrained transport and adaptive mesh refinement in the Black Hole Accretion Code,” *Astronomy & Astrophysics* **629**, A61 (2019), publisher: EDP Sciences.
- [81] M. Abramowicz, M. Jaroszynski, and M. Sikora, “Relativistic, accreting disks.” *A&A* **63**, 221–224 (1978).
- [82] Phillip Colella and Paul R. Woodward, “The Piecewise Parabolic Method (PPM) for gas-dynamical simulations,” *Journal of Computational Physics* **54**, 174–201 (1984).
- [83] L. Del Zanna, O. Zanotti, N. Bucciantini, and P. Londrillo, “ECHO: a eulerian conservative high-order scheme for general relativistic magnetohydrodynamics and magnetodynamics,” *Astronomy & Astrophysics* **473**, 11–30 (2007), number: 1 Publisher: EDP Sciences.

- [84] Oliver Porth, Koushik Chatterjee, Ramesh Narayan, Charles F. Gammie, Yosuke Mizuno, Peter Anninos, John G. Baker, Matteo Bugli, Chi-kwan Chan, Jordy Davelaar, Luca Del Zanna, Zachariah B. Etienne, P. Chris Fragile, Bernard J. Kelly, Matthew Liska, Sera Markoff, Jonathan C. McKinney, Bhupendra Mishra, Scott C. Noble, Héctor Olivares, Ben Prather, Luciano Rezzolla, Benjamin R. Ryan, James M. Stone, Niccolò Tomei, Christopher J. White, Ziri Younsi, Kazunori Akiyama, Antxon Alberdi, Walter Alef, Keiichi Asada, Rebecca Azulay, Anne-Kathrin Baczko, David Ball, Mislav Baloković, John Barrett, Dan Bintley, Lindy Blackburn, Wilfred Boland, Katherine L. Bouman, Geoffrey C. Bower, Michael Bremer, Christiaan D. Brinkerink, Roger Brissenden, Silke Britzen, Avery E. Broderick, Dominique Brogiere, Thomas Bronzwaer, Do-Young Byun, John E. Carlstrom, Andrew Chael, Shami Chatterjee, Ming-Tang Chen, Yongjun Chen, Ilje Cho, Pierre Christian, John E. Conway, James M. Cordes, B. Crew Geoffrey, Yuzhu Cui, Mariafelicia De Laurentis, Roger Deane, Jessica Dempsey, Gregory Desvignes, Sheperd S. Doeleman, Ralph P. Eatough, Heino Falcke, Vincent L. Fish, Ed Fomalont, Raquel Fraga-Encinas, Bill Freeman, Per Friberg, Christian M. Fromm, José L. Gómez, Peter Galison, Roberto García, Olivier Gentaz, Boris Georgiev, Ciriaco Goddi, Roman Gold, Minfeng Gu, Mark Gurwell, Kazuhiro Hada, Michael H. Hecht, Ronald Hesper, Luis C. Ho, Paul Ho, Mareki Honma, Chih-Wei L. Huang, Lei Huang, David H. Hughes, Shiro Ikeda, Makoto Inoue, Sara Issaoun, David J. James, Buell T. Jannuzi, Michael Janssen, Britton Jeter, Wu Jiang, Michael D. Johnson, Svetlana Jorstad, Taehyun Jung, Mansour Karami, Ramesh Karuppusamy, Tomohisa Kawashima, Garrett K. Keating, Mark Kettenis, Jae-Young Kim, Junhan Kim, Jongsoo Kim, Motoki Kino, Jun Yi Koay, M. Koch Patrick, Shoko Koyama, Michael Kramer, Carsten Kramer, Thomas P. Krichbaum, Cheng-Yu Kuo, Tod R. Lauer, Sang-Sung Lee, Yan-Rong Li, Zhiyuan Li, Michael Lindqvist, Kuo Liu, Elisabetta Liuzzo, Wen-Ping Lo, Andrei P. Lobanov, Laurent Loinard, Colin Lonsdale, Ru-Sen Lu, Nicholas R. MacDonald, Jirong Mao, Daniel P. Marrone, Alan P. Marscher, Iván Martí-Vidal, Satoki Matsushita, Lynn D. Matthews, Lia Medeiros, Karl M. Menten, Izumi Mizuno, James M. Moran, Kotaro Moriyama, Monika Moscibrodzka, Cornelia Müller, Hiroshi Nagai, Neil M. Nagar, Masanori Nakamura, Gopal Narayanan, Iniyana Natarajan, Roberto Neri, Chunchong Ni, Aristeidis Noutsos, Hiroki Okino, Tomoaki Oyama, Feryal Özel, Daniel C. M. Palumbo, Nimesh Patel, Ue-Li Pen, Dominic W. Pesce, Vincent Piétu, Richard Plambeck, Aleksandar PopStefanija, Jorge A. Preciado-López, Dimitrios Psaltis, Hung-Yi Pu, Venkatesh Ramakrishnan, Ramprasad Rao, Mark G. Rawlings, Alexander W. Raymond, Bart Ripperda, Freek Roelofs, Alan Rogers, Eduardo Ros, Mel Rose, Arash Roshanineshat, Helge Rottmann, Alan L. Roy, Chet Ruszczyk, Kazi L. J. Rygl, Salvador Sánchez, David Sánchez-Arguelles, Mahito Sasada, Tuomas Savolainen, F. Peter Schloerb, Karl-Friedrich Schuster, Lijing Shao, Zhiqiang Shen, Des Small, Bong Won Sohn, Jason SooHoo, Fumie Tazaki, Paul Tiede, Remo P. J. Tilanus, Michael Titus, Kenji Toma, Pablo Torne, Tyler Trent, Sascha Trippe, Shuichiro Tsuda, Ilse van Bemmelen, Huib Jan van Langevelde, Daniel R. van Rossum, Jan Wagner, John Wardle, Jonathan Weintroub, Norbert Wex, Robert Wharton, Maciek Wielgus, George N. Wong, Qingwen Wu, Ken Young, André Young, Feng Yuan, Ye-Fei Yuan, J. Anton Zensus, Guangyao Zhao, Shan-Shan Zhao, Ziyang Zhu, and (The Event Horizon Telescope Collaboration), “The Event Horizon General Relativistic Magneto-hydrodynamic Code Comparison Project,” *The Astrophysical Journal Supplement Series* **243**, 26 (2019), publisher: The American Astronomical Society.
- [85] Alexander Tchekhovskoy, Ramesh Narayan, and Jonathan C. McKinney, “Efficient generation of jets from magnetically arrested accretion on a rapidly spinning black hole,” *Monthly Notices of the Royal Astronomical Society: Letters* **418**, L79–L83 (2011).
- [86] Po Kin Leung, Charles F. Gammie, and Scott C. Noble, “NUMERICAL CALCULATION OF MAGNETO-BREMSSTRAHLUNG EMISSION AND ABSORPTION COEFFICIENTS,” *The Astrophysical Journal* **737**, 21 (2011), publisher: The American Astronomical Society.
- [87] Lakshmi Malvadi Shivakumar and Christoph Federrath, “Numerical viscosity and resistivity in MHD turbulence simulations,” *Monthly Notices of the Royal Astronomical Society* **537**, 2961–2986 (2025).
- [88] et al. Collaboration, Event Horizon Telescope, “First Sagittarius A* Event Horizon Telescope Results. V. Testing Astrophysical Models of the Galactic Center Black Hole,” *The Astrophysical Journal Letters* **930**, L16 (2022), publisher: IOP Publishing.
- [89] R. D. Blandford and D. G. Payne, “Hydromagnetic flows from accretion discs and the production of radio jets,” *Monthly Notices of the Royal Astronomical Society* **199**, 883–903 (1982).
- [90] et al. Collaboration, Event Horizon Telescope, “First Sagittarius A* Event Horizon Telescope Results. I. The Shadow of the Supermassive Black Hole in the Center of the Milky Way,” *The Astrophysical Journal Letters* **930**, L12 (2022), publisher: IOP Publishing.